JOURNAL OF PETROLOGY | VOLUME 40 | NUMBER 10 | PAGES 1509–1525 | 1999

Synthetic Fluid Inclusions XIV: Coexisting Silicate Melt and Aqueous Fluid Inclusions in the Haplogranite–H_2O–NaCl–KCl System

J. J. STUDENT AND R. J. BODNAR*

FLUIDS RESEARCH LABORATORY, DEPARTMENT OF GEOLOGICAL SCIENCES, VIRGINIA TECH, BLACKSBURG, VA, 24061-0420, USA

RECEIVED DECEMBER 18, 1998; REVISED TYPESCRIPT ACCEPTED APRIL 30, 1999

Coeval silicate melt and aqueous synthetic fluid inclusions were formed at 800°C and 2000 bars in the quartz-saturated haplogranite–H_2O–NaCl–KCl system. The equilibrium assemblage consisted of $Ab_{19·2}Or_{31·1}Qtz_{49·1}$ melt, quartz, and an aqueous solution with a composition of 7·4 wt % NaCl + 5·9 wt % KCl. The melt contained 0·18 wt % Cl^- and ~5·5 wt % H_2O. The calculated partition coefficient of chloride between the melt and aqueous fluid ($D_{Cl}^{m/aq} = C_{Cl}^{m}/C_{Cl}^{aq}$) is 0·021. The calculated distribution coefficient of Na and K between the melt and the aqueous phase $D_{Na/K}^{m/aq} = (C_{Na}^{m}/C_{K}^{m})/(C_{Na}^{aq}/C_{K}^{aq})$ is 0·40. Homogenization temperatures of synthetic silicate melt inclusions obtained by heating in 10·0°C/day increments in a tube furnace agreed with known formation temperatures, with no size dependence. When measured in a high-temperature heating stage, a heating rate of 1°C/min produced homogenization temperatures that were about 10°C lower than those obtained from the same inclusions using a heating rate of 3°C/min, although both heating rates produced homogenization temperatures above the formation temperature. A positive correlation between inclusion size and T_h was observed for both heating rates. Results confirm that microthermometric data from coeval silicate melt and aqueous fluid inclusions can be used to accurately predict P–T *formation conditions if data from the smallest melt inclusions are used, or if the melt inclusions are homogenized using a slow heating rate (<1°C/min).*

KEY WORDS: *distribution coefficient; haplogranite; melt inclusions; synthetic fluid inclusions; microthermometry*

INTRODUCTION

In recent years the study of silicate melt inclusions has gained considerable popularity as a method to characterize the *PTX* evolution of igneous processes (Anderson, 1974; Roedder, 1979; Lowenstern, 1995). Of special interest has been the study of melt inclusions trapped in an immiscible fluid–melt system (Roedder, 1979, 1984, 1992; Hansteen & Lustenhouwer, 1990; Frezzotti, 1992; Naumov *et al.*, 1992, 1996; Yang & Bodnar, 1994; Student & Bodnar, 1996). Microthermometric data from such inclusions can be used directly to determine formation temperatures and pressures, without the necessity of invoking difficult to prove assumptions or requiring an independent geobarometer or geothermometer (Roedder & Bodnar, 1980).

Roedder (1992) described specific types of magmatic immiscibility (immiscibility being defined as the existence of two or more non-crystalline, multi-component solutions which differ in properties and composition at equilibrium), including silicate melt–silicate melt, silicate melt–sulfide melt and silicate melt–aqueous fluid. In this study we have investigated the behavior of synthetic fluid inclusions trapped under conditions of silicate melt–aqueous fluid immiscibility in the haplogranite–H_2O–NaCl–KCl system. We interpreted microthermometric data obtained from melt inclusions trapped in quartz using phase equilibrium data for the haplogranite–H_2O system from Tuttle & Bowen (1958), ignoring the potential effect of chloride on the phase relationships (see Koster van Groos & Wyllie, 1969; Webster, 1992). The compositions of aqueous inclusions

*Corresponding author. Telephone: +1-540-231-7455. Fax: +1-540-231-3386. e-mail: bubbles@vt.edu

trapped in equilibrium with the melt were interpreted using data from Hall *et al.* (1988), Sterner *et al.* (1988) and Bodnar *et al.* (1989). The *P–T* path for the aqueous inclusion isochore was calculated using *PVTX* data from Bodnar & Vityk (1994).

EXPERIMENTAL PROCEDURES

The technique used to produce synthetic melt and aqueous inclusions in this study is a modification of the technique described by Sterner & Bodnar (1984) and Bodnar & Sterner (1987) for aqueous fluid inclusions. Quartz cores ~4 mm in diameter were cut from optical grade, inclusion-free Brazilian quartz crystals. The cores were then fractured using a thermal shock technique, as described by Bodnar & Sterner (1987). Melt and aqueous inclusions were formed at elevated temperature and pressure when small droplets or thin films of melt and aqueous solution were trapped during the fracture-healing process. Some inclusions were also trapped when new quartz precipitated on the outer rim of the quartz core during the experiment, and when new quartz microphenocrysts nucleated and grew during the run, as described below.

The quartz core, along with materials to produce the melt and aqueous solution, were loaded into platinum capsules of 5 mm OD × 4 cm length. The haplogranite melt starting material was a mixture of silica gel and $Ab_{25}Or_{75}$ fused glass. The bulk composition, represented by point 'A' in Fig. 1, includes the silica gel, the $Ab_{25}Or_{75}$ fused glass, and the quartz core. Before loading, the silica gel was dehydrated in a 1 atm muffle furnace at 900°C overnight. The $Ab_{25}Or_{75}$ glass was dried at a lower temperature (600°C) for several hours. Previous work had shown that this temperature was sufficiently high to drive off any adsorbed water from the glass without causing sodium loss. The $Ab_{25}Or_{75}$ glass was prepared for an earlier study (Voigt *et al.*, 1981) using techniques described by Hamilton & Henderson (1968). The 10 wt % NaCl aqueous solution was prepared from steam-distilled, deionized H_2O and ultrapure grade NaCl.

The starting materials were loaded into the Pt capsules in the following order: silica gel, $Ab_{25}Or_{75}$ fused glass, 10 wt % NaCl solution, and pre-fractured quartz core. Approximately 1 g (total) of starting material was used with a solid:fluid weight ratio of ~3:1. The weight of each component was pre-determined based on phase relationships for the water-saturated haplogranite system at 800°C and 2000 bars (Tuttle & Bowen, 1958) as shown in Fig. 1. The amount of silica gel used was in excess of the amount needed to produce the equilibrium melt composition at run conditions (see Fig. 1). Excess silica was added to assure that quartz would be a stable phase on the liquidus at run conditions and thus promote

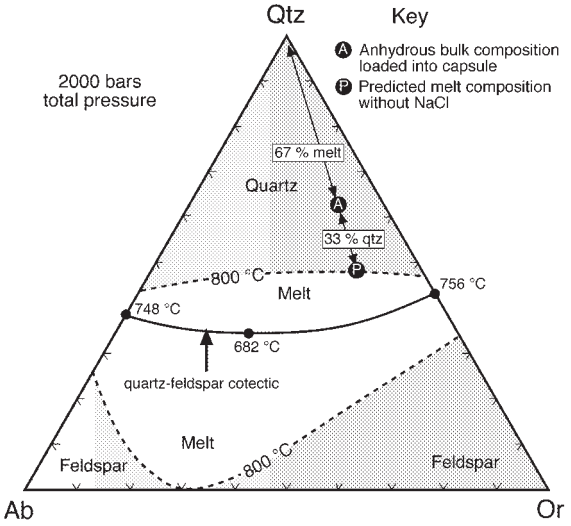

Fig. 1. The H_2O-saturated haplogranite ternary system at 2000 bars (after Tuttle & Bowen, 1958). The 800°C isotherm is shown with a dashed line. The stability fields for quartz and alkali feldspar at 800°C are represented by the shaded areas labeled 'Quartz' and 'Feldspar', respectively. The unshaded region represents the melt field at 800°C. The minimum melting temperature is 682°C on the quartz–alkali feldspar cotectic (bold line). Eutectic minima for quartz–albite and quartz–orthoclase are shown at 748°C and 756°C, respectively. Point 'A' represents the anhydrous starting composition used in this study, including all components except the H_2O–NaCl solution. Point 'P' represents the predicted melt composition at 800°C based on the starting anhydrous bulk composition and assuming no exchange of sodium and potassium between melt and aqueous phase. For a starting composition of 'A', quartz, melt of composition 'P', and water coexist at 800°C and 2000 bars. For the bulk composition 'A', the system contains 67 wt % melt and 33 wt % quartz at run conditions.

the healing of fractures and the precipitation of additional quartz onto the quartz core. Immediately after addition of the NaCl solution and quartz core, the capsules were sealed using an arc welder. The sealed capsules were weighed, placed in a vacuum oven at 100°C for several hours, and then reweighed to check for leakage.

The sealed capsules were placed in horizontal cold-seal type vessels and heated–pressurized to avoid the NaCl–H_2O two-phase region (see Bodnar *et al.*, 1985). The run was stabilized at 2000 bars and 800°C within 35 min of initial heat-up and maintained at that condition for 7 days. During the quench, the pressure was maintained at 2000 bars during cooling to 450°C (slightly below the glass transition temperature; Romano *et al.*, 1994) to help prevent loss of water from the melt and to avoid the NaCl–H_2O two-phase region (Bodnar *et al.*, 1985). The pressure was then decreased to 1000 bars and allowed to further decrease with temperature to ambient conditions to avoid rupturing the Pt capsule.

After removing the capsules from the pressure vessel, the capsules were cleaned and weighed to check for leakage during the run. Although four different samples were run, all results described below are from a single

sample. The other three samples were not used because the number and size of the melt inclusions in these samples was insufficient for electron microprobe analysis or to obtain a statistically valid number of data points. Why only one experiment produced large numbers of both aqueous and melt inclusions, whereas the other three did not, is unclear at this time. However, the three experiments in which melt inclusions were small and/or rare did not include silica gel in the starting material. In the three experiments without silica gel numerous aqueous fluid inclusions were trapped, but very few melt inclusions formed. Moreover, the abundance, aperture and geometry of fractures in the original quartz core are not easily controlled. Failure to form abundant, large melt inclusions in three samples may be related to all of these factors.

After completion of the run, the experimental charge consisted of a single tubule of 3·5 cm length containing a mixture of haplogranite glass and quartz microphenocrysts, with the quartz core attached to one end (Fig. 2a). Disks ~1 mm thick were sliced from the quartz core as well as from the haplogranite glass + quartz microphenocryst portion of the charge, mounted on a glass slide, and doubly polished for petrographic observation. Each disk was examined optically to determine the inclusion distribution and textural features. Following microthermometric analysis to homogenize the inclusions, selected glass inclusions (often containing bubbles that reappeared during the quench) were exposed at the surface by further grinding and polishing in preparation for glass (melt) analysis by electron microprobe and secondary ion mass spectrometry (SIMS).

Aqueous fluid inclusions trapped in the quartz core were analyzed with a US Geological Survey (USGS)-type gas flow heating–freezing stage (Werre *et al.*, 1979). The stage was calibrated at −56·6°C, 0·0°C, 374·1°C and 573°C using synthetic fluid inclusions and the quartz α–β transition. The accuracy and precision for temperatures ≤0·0°C are ±0·1°C, and ±1·0°C for temperatures between 100 and 500°C. Salinities and sodium-to-potassium ratios of aqueous inclusions were calculated based on the sylvite dissolution temperature and the final ice-melting temperature, interpreted within the H_2O–NaCl–KCl ternary (Hall *et al.*, 1988; Sterner *et al.*, 1988; Bodnar *et al.*, 1989). The average ice-melting temperature and liquid–vapor homogenization temperature were used to calculate an NaCl-equivalent salinity (Bodnar, 1993) and isochore (Bodnar & Vityk, 1994) for the aqueous inclusions. Bodnar (1983) had previously shown that the *PVT* properties of mixed electrolyte systems are reasonably well approximated by the *PVT* properties of an NaCl solution having the same freezing-point depression as that of the mixed electrolyte.

Silicate glass inclusions in the quartz core were analyzed on a Linkam TS1500 heating stage. The stage is mounted on an Olympus BX60 microscope equipped with an 80 × objective. With this arrangement, features as small as 1–2 μm are easily resolved. The stage was calibrated at the critical temperature of H_2O (374·1°C), the melting point of ultrapure NaCl (801°C), and the melting point of silver (961°C). The accuracy and precision of homogenization temperatures of melt inclusions is estimated at better than ±5°C. The stage was flushed with an argon + 1% H_2 gas mixture during heating to minimize oxidation. From room temperature to 400°C, a heating rate of 30°C/min was used. The rate was slowed to 10°C/min from 400 to 600°C and then held at that temperature for 30 min before proceeding with homogenization runs.

Three different heating procedures were followed to measure the homogenization temperatures of melt inclusions. For one sample, a heating rate of 3°C/min was used above 600°C, except that the temperature was held constant for a few minutes several times during the heating run to photograph the inclusions. Additionally, near the homogenization temperature, it was necessary to thermally cycle the sample by several degrees to confirm that the bubble had indeed disappeared. If, during cooling, the bubble immediately grew back at the same location where it was last observed, it was assumed that homogenization was not achieved. If the bubble did not reappear with several degrees of cooling, or if the bubble reappeared in a different area of the inclusion, it was assumed that homogenization had been achieved. This thermal cycling technique is similar to that used to study small aqueous inclusions, where it has been found to produce accurate and reproducible homogenization temperatures (Goldstein & Reynolds, 1994).

The terminology used in the literature to describe the bubbles that occur in silicate melt inclusions is inconsistent and, often, confusing. Bubbles in silicate melt inclusions may have at least four different origins. If the melt is saturated in a volatile phase, the inclusion may trap both melt and vapor to produce a vapor (or fluid) bubble in the resultant inclusion. Or, if the inclusion traps only a volatile-bearing melt phase, the melt may become saturated in the volatile component and exsolve a separate fluid phase during cooling, producing a bubble in the melt inclusion. If the inclusion traps a volatile-free melt (or one with a low concentration of volatiles) the melt may not become saturated in the volatile component during cooling. But, owing to the different coefficients of thermal expansion and compressibility of the melt and its host mineral, the melt (glass) volume will decrease more than the mineral during cooling, producing a void space that is essentially a vacuum in the inclusion. Finally, a melt inclusion may leak with loss of some melt before the inclusion is completely sealed, leaving behind an inclusion with bubble. This process often occurs with hourglass inclusions (Anderson, 1991; Lowenstern, 1995).

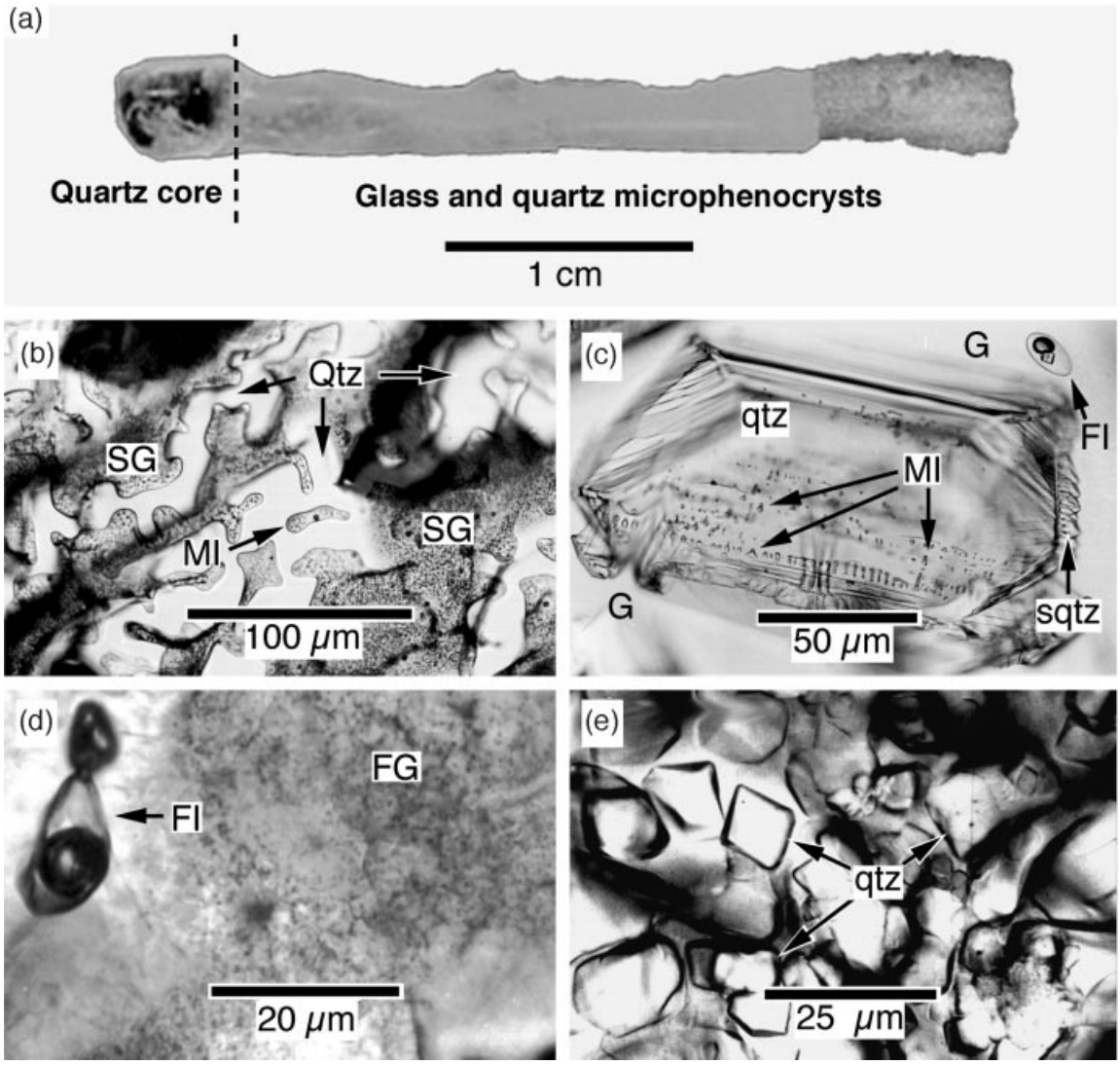

Fig. 2. Textures observed in the run product. (a) The experimental charge showing the quartz core at the far left and the glass + quartz microphenocryst assemblage to the right. The darker gray area at the far right consists mostly of microphenocrysts of quartz. (b) Sheets of glass (SG) with numerous bubbles trapped beneath a quartz overgrowth on the quartz core (Qtz). Necking down of the sheet has formed an isolated melt inclusion (MI). (c) Clear haplogranite glass (G), isolated $FIA_{(aq)}$ 2 inclusions (FI), and quartz microphenocryst (qtz). The quartz microphenocrysts are rimmed with skeletal quartz (sqtz). The microphenocryst contains $FIA_{(mlt)}$ 2 inclusions (MI). (d) Milky glass (FG) containing numerous quench bubbles. An $FIA_{(aq)}$ 2 inclusion (FI) occurs in the upper left-hand corner. (e) Abundant quartz microphenocrysts (qtz) in clear haplogranite glass.

To avoid confusion, we use the term 'bubble' or 'vapor bubble' to refer to any approximately spherical (non-glassy) void within a melt inclusion, with no genetic or compositional implications. In some cases, we use the term 'quench bubbles' to describe small, uniformly distributed bubbles that presumably form by exsolution of water from the melt during the quench, as reported by Burnham & Jahns (1962). We recognize, however, that in reality all of the bubbles in the melt inclusions, except for those rare examples of heterogeneous trapping of melt plus fluid, are in fact 'quench bubbles'.

Homogenization temperatures of melt inclusions in a second quartz wafer were measured using two different heating rates. First, a heating rate of 1°C/min was used for heating above 600°C, and this rate was maintained until the last inclusion homogenized at 853°C. The sample was then cooled to 600°C, where the temperature was maintained for 30 min. The sample was then reheated at 3°C/min until the last inclusion homogenized at 863°C. In both cases, heating rates were constant above 600°C and the inclusions were not thermally cycled—this could lead to an underestimation of the homogenization temperature by a few degrees, based on results from the earlier experiment in which thermal cycling was used. In all cases, a bubble reappeared during cooling following homogenization.

A third quartz wafer containing glass inclusions was incrementally heated in a 1 atm vertical tube furnace. The wafer was placed in a Pt holder and suspended from the top of the furnace. The sample was positioned within the 'hot spot' of the furnace, where previous tests had determined a thermal gradient of ± 5°C over a distance of ± 8 cm from the center of the 'hot spot'. The furnace thermocouple was calibrated using pure silver at 961°C, and at lower temperatures this thermocouple was calibrated against another well-calibrated thermocouple. The accuracy and precision of temperature measurements at 800°C is estimated at ± 10°C. The sample was initially placed in the pre-heated furnace at 750°C for a period of 1 day. After 1 day, the sample was rapidly quenched in water at a rate >800°C/s and observed with a petrographic microscope. The procedure was repeated with a 10°C increase in temperature each day until the quenched inclusions contained only a single glass phase following quenching, indicating that the inclusions were homogenized at run conditions. It should be noted that, unlike the experiments conducted in the microscope heating stage in which vapor bubbles were generated during the relatively slow cooling, the cooling rate for the furnace experiments was sufficiently high to prohibit formation of bubbles during cooling, once homogenization was achieved.

Electron microprobe analyses were performed on a Cameca SX50 electron microprobe, equipped with both wave and energy dispersive spectrometers (WDS and EDS, respectively) at Virginia Tech. Quantitative analyses were conducted using WDS. Analysis and standardization were performed using silicate, oxide and phosphate standards, and the data were corrected using PAP method according to Pouchou & Pichoir (1985) using vendor-supplied software. Standard deviations (1σ) based on Benson orthoclase and Amelia albite standards, respectively, are as follows: SiO_2 $\pm 0{\cdot}49$ and $\pm 0{\cdot}59$ wt %; Al_2O_3 $\pm 0{\cdot}22$ and $\pm 0{\cdot}23$ wt %; K_2O $\pm 0{\cdot}26$ and $\pm 0{\cdot}04$ wt %; Na_2O $\pm 0{\cdot}04$ and $\pm 0{\cdot}26$ wt %; and Cl^- $\pm 0{\cdot}01$ and $\pm 0{\cdot}02$ wt % (Table 1). Standard deviation (1σ) for Cl^- in a Durango apatite standard is $\pm 0{\cdot}01$ wt %. Analyses were performed at 15 kV, using a current of 2 nA with a 2 μm rastered beam. Counting times and analytical sequence were as follows: Na_2O, 10 s; K_2O, 10 s; Cl^-, 15 s; Al_2O_3, 20 s; and SiO_2, 20 s. These beam conditions and analytical sequence resulted in non-detectable volatilization and migration of Na, K, and Cl for the first analysis conducted at a single spot location on standard samples. Larger melt inclusions were analyzed multiple times (up to three) when previous spot analysis locations within the inclusion could be avoided.

SIMS analyses were performed on a Cameca 6F ion-probe with a cesium gun at the Department of Terrestrial Magnetism at the Carnegie Institution of Washington. The elements H and Cl were analyzed *in situ* using a 10 kV primary beam of Cs^+ with a current of 3–8 nA and a beam diameter of 20–30 μm (Hauri *et al.*, 1999). Secondary ions were analyzed at an accelerating voltage of +5 kV. A small field aperture of 8 μm diameter was inserted into the secondary ion beam to filter out edge effects. Secondary ions were referenced to counts of ^{30}Si with an analytical uncertainty of $\pm 10\%$ in terms of ^{1}H:^{30}Si and ^{35}Cl:^{30}Si. Si concentrations were previously determined by electron microprobe. Only five melt inclusions were large enough for analysis without producing an edge effect from the host quartz.

RESULTS

Sample description

The run product consists of the quartz core at one end of the charge, with a heterogeneous mixture of glass and quartz microphenocrysts forming the majority of the sample (Fig. 2a). The quartz core contains healed fractures with either aqueous fluid inclusions or silicate glass inclusions. Some rare fractures contain both types of inclusions. A similar inclusion distribution, with many fractures containing inclusions of a single type, was observed for inclusions trapped in the two-phase (liquid + vapor) field in the H_2O–NaCl system by Bodnar *et al.* (1985). Relatively fewer fractures were observed which contained both liquid-rich and vapor-rich inclusions. However, the compositions of inclusions in fractures containing only liquid-rich or only vapor-rich inclusions were identical to compositions of similar inclusions found in less-abundant fractures containing both types of inclusions. Bodnar *et al.* (1985) interpreted this behavior to indicate that even though many fractures contained inclusions of only a single type, the composition of those inclusions was representative of one or the other of the two immiscible phases present at run conditions. On the basis of that analogy, as well as the excellent agreement between observed and expected compositions described below, we interpret the compositions of the aqueous and melt inclusions in the quartz host to be representative of the equilibrium melt and aqueous fluid phases present at 800°C and 2000 bars.

Sheets of glass (originally films of melt) and isolated glass inclusions occur within healed fractures in the quartz core (Fig. 2b). Often the glass- (melt-)filled fractures are not completely isolated within the quartz core but, rather, are connected to the surface. These glass sheets commonly contain small (<1 μm) bubbles.

Some areas of the charge show clear haplogranite glass that preserves isolated quartz microphenocrysts and aqueous fluid inclusions (Fig. 2c). The quartz microphenocrysts occur in a range of sizes (15–250 μm) and shapes, and sometimes contain glass inclusions. In other regions of the charge, the glass is milky with fewer quartz microphenocrysts and aqueous fluid inclusions compared with

Table 1: Electron microprobe data (in wt %) for oxides and Cl^- for melt inclusions and matrix glass

Sample	SiO_2	Al_2O_3	Na_2O	K_2O	Cl^-	Total	Ab	Or	Qtz	C	NaKMS	Total	*n*
Silicate melt inclusions													
MI E	75·27	8·65	2·57	5·39	0·17	92·03	20·3	29·8	47·7		2·2	100·0	*3*
MI D	75·35	8·69	2·63	5·46	0·17	92·30	20·5	29·7	47·4		2·3	100·0	*3*
MI A	75·45	8·70	2·61	5·33	0·17	92·23	20·7	29·6	47·6		2·1	100·0	*3*
MI H	75·94	8·72	2·01	4·86	0·18	91·67	18·6	31·4	49·9	0·2		100·0	*3*
MI B	76·33	8·63	2·10	5·18	0·18	92·41	18·3	31·6	49·4		0·7	100·0	*2*
MI G	76·35	8·64	1·94	4·84	0·18	91·92	17·9	31·2	50·7	0·2		100·0	*3*
MI C	76·43	8·61	1·94	4·89	0·17	92·02	17·9	31·4	50·5	0·1		100·0	*3*
MI I	76·97	9·16	2·08	5·06	0·19	93·39	18·9	32·1	48·8	0·3		100·0	*1*
MI F	77·17	8·76	2·06	4·99	0·18	93·16	18·7	31·6	49·7		0·0	100·0	*1*
Average	76·14	8·73	2·22	5·11	0·18	92·37	19·2	31·1	49·1		0·7	100·0	*9*
Max.	77·17	9·16	2·63	5·46	0·19	94·24	20·7	32·1	50·7				
Min.	75·27	8·61	1·94	4·84	0·17	91·67	17·9	29·6	47·4				
SD	0·69	0·17	0·30	0·24	0·01	0·57	1·1	1·0	1·3				*9*
Silicate melt and matrix glass with excess SiO_2 from quartz													
MI J	76·53	8·41	1·29	4·12	0·09	90·43	12·0	27·0	59·0	2·0		100·0	*2*
MI K	77·59	8·74	1·61	4·16	0·08	92·18	14·8	26·7	56·8	1·7		100·0	*2*
MI L	76·26	8·42	1·77	4·63	0·10	91·16	16·4	30·0	53·0	0·6		100·0	*2*
gla4	74·44	10·92	1·56	4·12	0·14	91·18	14·5	26·7	54·5	4·3		100·0	*1*
Matrix glass													
gla22	71·77	10·65	2·99	6·20	0·15	91·77	25·3	36·6	36·6		1·5	100·0	*1*
gla21	72·08	11·06	3·11	6·42	0·13	92·80	26·0	37·5	34·9		1·5	100·0	*1*
gla32	72·45	10·80	3·02	6·22	0·16	92·65	25·5	36·7	36·5		1·4	100·0	*1*
gla28	72·67	10·72	3·20	6·18	0·15	92·93	26·2	35·3	36·7		1·9	100·0	*1*
gla27	73·43	10·85	3·06	6·13	0·17	93·65	25·8	36·0	37·0		1·2	100·0	*1*
gla33	73·73	10·94	2·34	5·67	0·12	92·80	21·4	36·2	41·5	1·0		100·0	*1*
gla5	73·74	10·98	2·49	5·75	0·12	93·07	22·7	36·6	40·1	0·7		100·0	*1*
gla42	73·89	11·19	2·43	5·87	0·10	93·49	22·0	37·1	39·9	0·9		100·0	*1*
gla43	73·93	10·64	2·38	5·59	0·12	92·67	21·8	35·7	41·8	0·7		100·0	*1*
gla36	74·04	10·67	2·07	4·95	0·16	91·89	19·1	31·9	46·9	2·1		100·0	*1*
gla10	74·19	10·70	2·34	5·19	0·14	92·56	21·4	33·2	44·1	1·3		100·0	*1*
gla41	74·24	11·11	2·04	4·62	0·13	92·14	18·8	29·7	48·6	3·0		100·0	*1*
gla1	74·45	10·60	2·39	5·64	0·17	93·25	21·7	35·8	41·9	0·6		100·0	*1*
gla3	74·76	10·19	2·37	5·68	0·12	93·13	21·6	36·1	42·2	0·2		100·0	*1*
gla39	74·79	10·30	2·45	5·58	0·11	93·23	22·3	35·4	42·1	0·2		100·0	*1*
gla17	74·85	8·68	2·48	5·51	0·17	91·67	19·8	30·7	47·4		2·1	100·0	*1*
gla15	75·30	9·02	2·55	5·53	0·12	92·52	20·7	31·3	46·2		1·8	100·0	*1*
gla9	75·54	10·00	2·34	5·20	0·11	93·20	21·3	33·0	45·2	0·6		100·0	*1*
gla24	75·64	9·21	2·44	5·46	0·15	92·90	20·7	32·3	46·0		1·1	100·0	*1*
gla31	75·66	9·04	2·74	5·63	0·14	93·21	21·2	30·5	45·9		2·3	100·0	*1*
gla26	75·72	8·84	2·75	5·54	0·15	93·00	21·1	29·6	46·8		2·5	100·0	*1*
gla6	75·78	8·57	2·09	4·95	0·17	91·56	18·9	31·2	49·6		0·3	100·0	*1*
gla35	75·82	9·57	2·21	5·47	0·11	93·19	20·1	34·7	45·2			100·0	*1*
gla29	75·89	8·54	2·59	5·30	0·17	92·50	20·3	29·0	48·5		2·2	100·0	*1*
gla14	75·97	8·94	2·12	5·18	0·16	92·38	19·1	32·6	48·0		0·2	100·0	*1*
gla8	76·04	8·55	2·08	4·99	0·12	91·77	18·6	31·2	49·8		0·4	100·0	*1*
gla7	76·05	8·58	2·05	4·88	0·18	91·75	18·8	31·2	49·9		0·1	100·0	*1*
gla2	76·20	8·89	2·13	4·94	0·17	92·34	19·6	31·7	48·7			100·0	*1*

Sample	SiO_2	Al_2O_3	Na_2O	K_2O	Cl^-	Total	Ab	Or	Qtz	C	NaKMS	Total	*n*
gla16	76·20	8·67	2·24	5·09	0·15	92·34	19·4	30·8	49·1		0·8	100·0	*1*
gla25	76·36	8·90	2·10	5·05	0·14	92·53	19·2	32·2	48·6		0·0	100·0	*1*
gla13	76·40	8·44	2·12	4·84	0·14	91·93	18·9	30·1	50·5		0·4	100·0	*1*
gla18	76·45	8·50	2·26	5·22	0·13	92·56	18·8	30·3	49·6		1·3	100·0	*1*
gla34	76·57	9·37	2·13	5·26	0·12	93·45	19·3	33·3	47·2	0·2		100·0	*1*
gla12	76·58	9·15	2·06	5·14	0·17	93·10	18·8	32·7	48·3	0·2		100·0	*1*
gla40	76·64	9·25	2·31	5·12	0·14	93·47	20·7	32·1	47·0		0·1	100·0	*1*
gla11	76·69	8·88	2·17	5·17	0·17	93·09	19·1	31·9	48·6		0·4	100·0	*1*
gla19	76·79	8·67	2·15	5·02	0·13	92·76	19·0	31·0	49·6		0·5	100·0	*1*
gla37	76·97	9·06	2·26	5·02	0·17	93·49	20·3	31·5	48·1		0·1	100·0	*1*
gla38	76·97	8·54	2·13	5·00	0·14	92·78	18·6	30·5	50·2		0·6	100·0	*1*
gla30	76·98	8·96	2·29	5·04	0·09	93·37	20·2	31·0	48·4		0·4	100·0	*1*
gla20	77·04	8·81	2·08	5·12	0·14	93·20	18·6	32·0	49·2		0·2	100·0	*1*
gla23	78·01	8·90	2·13	5·06	0·14	94·24	19·0	31·5	49·4		0·1	100·0	*1*
Average	75·26	9·59	2·39	5·39	0·14	92·78	21·5	33·8	44·5		0·3	100·0	*42*
Max.	78·01	11·19	3·20	6·42	0·18	94·24	26·2	37·5	50·5				
Min.	71·77	8·44	2·04	4·62	0·09	91·56	18·6	29·0	34·9				
SD	1·50	0·96	0·32	0·43	0·02	0·61	2·2	2·4	4·5				*42*
Electron microprobe standards													
Albite	0·59	0·23	0·25	0·04	0·02	SD							*32*
Orthoclase	0·49	0·22	0·04	0·26	0·01	SD							*29*

The sum of albite (Ab), orthoclase (Or), quartz (Qtz), corundum (C), and sodium–potassium metasilicate [NaKMS: $(NaK)_2SiO_3$] has been normalized to 100 wt % in terms of SiO_2, Al_2O_3, Na_2O and K_2O concentrations.
NaKMS is calculated as a mixture of Na_2SiO_3 and K_2SiO_3 with Na:K equal to microprobe results and the Na:K in the haplogranite components albite and orthoclase. Four of the analyses yielded unreasonably high Qtz values and indicate heterogeneous analysis of both melt and surrounding quartz. Standard deviations (1σ) are based on analyses of Amelia albite and Benson orthoclase standards.

the clear glass. The opacity of the glass is due to the presence of numerous small quench bubbles (Fig. 2d). The end of the charge opposite from the quartz core consists of quartz microphenocrysts (<20 μm in length) fused together by haplogranite glass (Fig. 2e). This represents the end of the capsule which originally contained silica gel, and the microphenocrysts represent a portion of the excess silica gel that has crystallized to quartz.

Aqueous fluid inclusions

Two aqueous fluid inclusion assemblages ($FIA_{(aq)}$ 1 and 2) are preserved in the charge. $FIA_{(aq)}$ 1 is preserved in healed fractures in the quartz core. These inclusions have a mature morphology, consisting of either well-rounded or negative-crystal forms (Fig. 3a). At room temperature, the inclusions contain two phases, liquid and vapor, in approximately equal volumetric proportions (Fig. 3c). $FIA_{(aq)}$ 2 occurs in the glass portion of the charge away from the quartz core. These inclusions contain variable volumetric proportions of liquid and vapor, ± halite ± rare, highly birefringent needles of muscovite (based on the petrographic characteristics of the needles) (Fig. 3d–g). The inclusions are typically flattened and elongated with compressed (deformed) bubbles. The long axis of the inclusions is usually parallel to the long axis of the charge. A halo of smaller bubbles (<1·0 μm) commonly occurs around $FIA_{(aq)}$ 2 inclusions (Fig. 3f) in the haplogranite glass. The bubbles may be related to loss of water from the aqueous inclusions to the glass during the relatively slow quenching used in our inclusion synthesis experiments, as has been reported by Romano *et al.* (1994). Water loss from the aqueous inclusions might also explain the highly variably salinities of the inclusions in glass, including the presence of some inclusions with halide daughter minerals (Fig. 3d, e, g). Alternatively, Davis & Ihinger (1998) have reported the heterogeneous nucleation of lithium disilicate crystals on bubbles in supercooled melt, and the halide crystals in bubbles observed in this study may have a similar origin.

Silicate melt inclusions

Silicate glass inclusions occur in healed fractures in the quartz core, beneath an overgrowth layer on the quartz core, and in quartz microphenocrysts throughout the

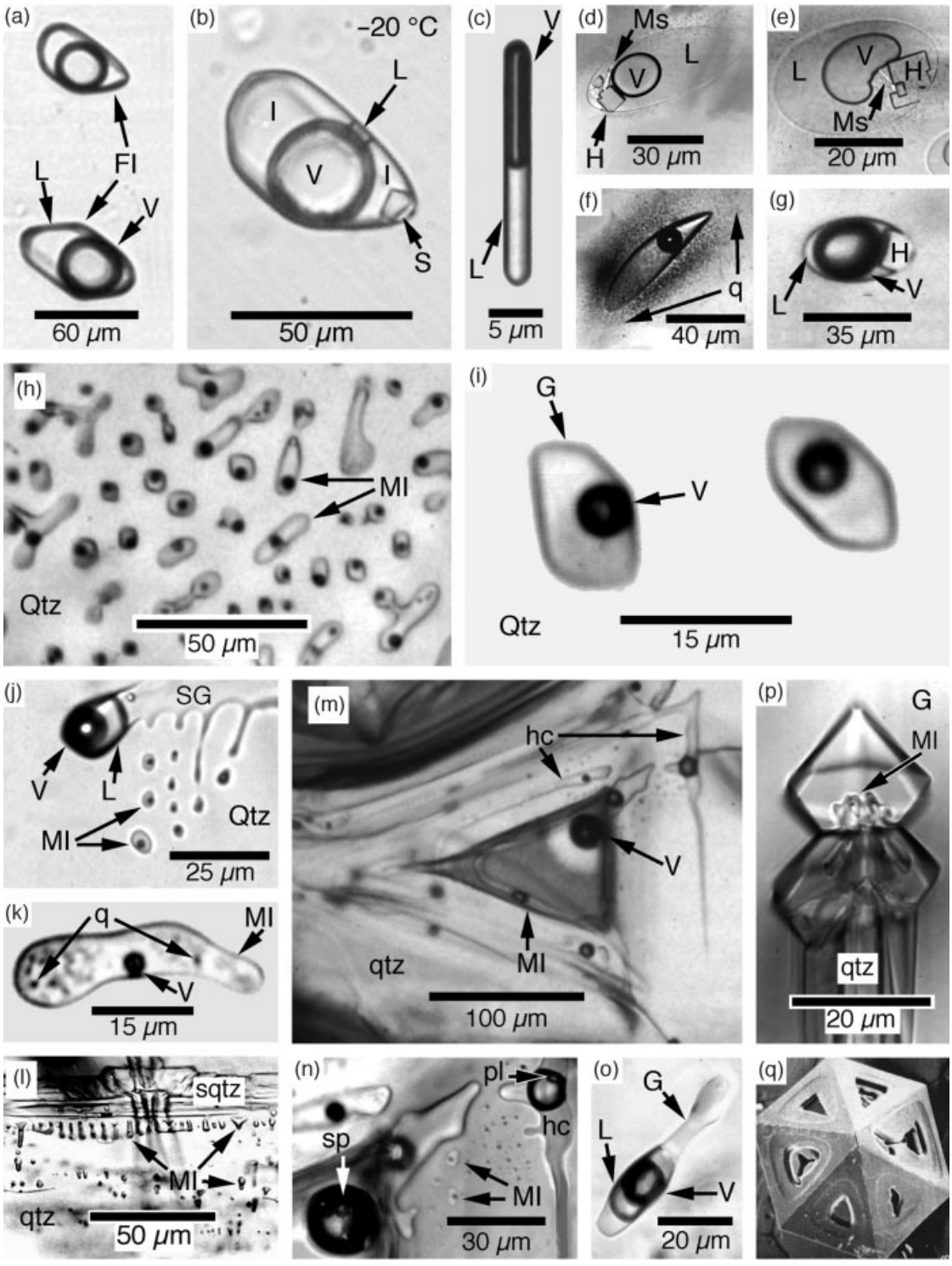

Fig. 3. Representative aqueous and silicate melt inclusions. (a) Two rounded to negative-crystal form $FIA_{(aq)}$ 1 inclusions (FI). Each inclusion contains an aqueous liquid (L) surrounding a vapor bubble (V). (b) Photograph at −20°C of the same inclusion as shown at the top of (a). The inclusion contains a vapor bubble (V), ice (I), liquid (L) and sylvite (S). (c) Acicular-shaped $FIA_{(aq)}$ 1 inclusion with nearly equal volumetric proportions of aqueous liquid (L) and vapor (V) at room temperature. (d) $FIA_{(aq)}$ 2 inclusion in haplogranite glass. The inclusion contains aqueous liquid (L) and vapor (V), several halite crystals (H), and muscovite (Ms). (e) $FIA_{(aq)}$ 2 inclusion in haplogranite glass. (Note the deformed vapor.) (f) $FIA_{(aq)}$ 2 inclusion in haplogranite glass. The inclusion contains aqueous liquid and vapor. [Note the quench bubbles (q) in the haplogranite glass surrounding the inclusion.] (g) $FIA_{(aq)}$ 2 inclusion in haplogranite glass. [Note the large volumetric proportion of vapor (V) and the halite

remainder of the charge. Inclusions associated with the quartz core are classified as melt fluid inclusion assemblage 1 ($FIA_{(mlt)}$ 1) and inclusions in quartz microphenocrysts are classified as $FIA_{(mlt)}$ 2. Melt inclusions from assemblage 1 are shown in Figs 2b and 3 (h, i, j, k and o). Inclusions from assemblage 2 are shown in Figs 2c and 3 (l, m, n and p). Inclusions from both $FIA_{(mlt)}$ 1 and $FIA_{(mlt)}$ 2 have similar phase ratios (glass to vapor) at room temperature and range in size from <1 μm to ~20 μm. One exceptionally large inclusion approaches 100 μm in maximum dimension (Fig. 3m).

Inclusions from $FIA_{(mlt)}$ 1 commonly have a negative-crystal form and contain a single vapor bubble. Typically the bubble constitutes ~15% of the inclusion area as seen in plan view (Fig. 3h and i). Melt inclusions that were trapped when quartz precipitated during fracture healing are shown in Fig. 3j. Aqueous fluid was also trapped in this fracture, as evidenced by an isolated two-phase aqueous inclusion at the boundary between quartz and glass. Aqueous liquid and vapor cannot be distinguished in the majority of bubbles observed in melt inclusions. Large inclusions (>30 μm) often contain one (or a few) large vapor bubbles as well as numerous smaller quench bubbles (Fig. 3k).

$FIA_{(mlt)}$ 2 inclusions occur within quartz microphenocrysts in the haplogranite glass. The inclusions are triangular, oblong and rounded in shape. Negative inclusion forms are not common as in $FIA_{(mlt)}$ 1. The majority of inclusions from $FIA_{(mlt)}$ 2 occur beneath quartz skeletal overgrowths on the microphenocrysts (Fig. 3l). The skeletal overgrowths are believed to have formed during quenching of the experiments. Such inclusions were classified as *zonal primary inclusions* by Sobolev & Kostyuk (1975). An especially large $FIA_{(mlt)}$ 2 inclusion (100 μm) is triangular in form and occurs on a rhombohedral prism of a quartz microphenocryst (Fig. 3m and n). Channels of glass–melt surround the inclusion and some of these channels contain several vapor bubbles. Aqueous liquid and vapor can be distinguished in some of the larger bubbles. Inclusions from $FIA_{(mlt)}$ 2 also occur in the interiors of the microphenocrysts. A mixed aqueous fluid–melt inclusion (heterogeneous) is shown in Fig. 3o. The inclusion trapped a heterogeneous mixture of both haplogranite melt and aqueous solution. Scepter-type quartz crystals with inclusions also occur (Fig. 3p). A natural β-quartz phenocryst from the Valley of Ten Thousand Smokes, Alaska (Clocchiatti, 1975) is shown in Fig. 3q for comparison.

Microthermometry

Aqueous fluid inclusions

The composition and density (isochore) of the aqueous inclusions were determined based on low-temperature phase behavior and the homogenization temperature, respectively. The inclusion compositions were interpreted using phase equilibrium data for the H_2O–NaCl–KCl system (Hall *et al.*, 1988; Sterner *et al.*, 1988; Bodnar *et al.*, 1989). The aqueous inclusions were first cooled to liquid nitrogen temperature (−196°C). During cooling the inclusions froze to an assemblage consisting of ice, hydrohalite ($NaCl{\cdot}2H_2O$) and sylvite. When heated from low temperature, $FIA_{(aq)}$ 1 shows first melting at approximately −22·6°C, in good agreement with the eutectic temperature for the system H_2O–NaCl–KCl, which is −22·9°C (Hall *et al.*, 1988). At the eutectic, the inclusions contain ice, sylvite and a liquid with the eutectic composition (20·24 wt % NaCl + 5·72 wt % KCl; Sterner *et al.*, 1988) (Fig. 3b). With continued heating, the inclusions follow the ice–sylvite cotectic until the sylvite completely disappears (Fig. 4). Sylvite dissolution temperatures ranged from −15·8° to −17·1°C. With continued heating, the inclusions follow a path from the ice–sylvite cotectic directly towards the H_2O apex as the remaining solid phase (ice) melts (Fig. 4). Final ice-melting temperatures ranged from −8·4 to −7·4°C with a mean value of −8·2°C for a group of 68 inclusions (Fig. 5, inset a). The intersection of the fluid inclusion path from the ice–sylvite cotectic to the H_2O apex with the −8·2°C isotherm defines the fluid inclusion composition of 7·4 wt % NaCl + 5·9 wt % KCl (Fig. 4). Solution compositions were calculated from the measured microthermometric data using the FORTRAN program

crystal (H).] (h) Plane of $FIA_{(mlt)}$ 1 inclusions (MI) along a fracture in the quartz core (Qtz). (i) Close-up of two $FIA_{(mlt)}$ 1 melt inclusions from the same plane of inclusions as shown in (h). The inclusions have a negative-crystal form. Each inclusion contains glass (G) and a vapor bubble (V) at room temperature. (j) Necking down of a sheet of melt–glass (SG) in a fracture in quartz (Qtz) to form isolated $FIA_{(mlt)}$ 1 inclusions (MI) and a single $FIA_{(aq)}$ 1 inclusion containing aqueous liquid (L) and vapor (V). (k) Oblong $FIA_{(mlt)}$ 1 inclusion (MI) with a vapor bubble (V) and smaller quench bubbles (q). (l) $FIA_{(mlt)}$ 2 inclusions (MI) trapped beneath a skeletal overgrowth (sqtz) on a quartz microphenocryst (qtz). (m) A triangular $FIA_{(mlt)}$ 2 inclusion (MI) trapped on a rhombohedral prism of a quartz microphenocryst (qtz). The inclusion is surrounded by helical channels (hc) of melt–glass. The inclusion glass appears dark from numerous small quench bubbles, except near the single, large vapor bubble (V). (n) Close-up of the vapor bubble and portions of the surrounding melt–glass channels (hc) from the inclusion shown in (m). The bubbles contain glass quench spheres (sp) and prismatic feldspar (pl). [Note the small glass inclusions (MI).] (o) Mixed inclusion (heterogeneous) containing H_2O-saturated haplogranite melt and aqueous fluid. The inclusion contains glass (G) surrounding a two-phase aqueous inclusion with liquid (L) and vapor (V) at room temperature. (p) Scepter quartz crystal (qtz) in glass (G). Six $FIA_{(mlt)}$ 2 inclusions (MI) occur on separate rhombohedral prisms near the top of the crystal. (q) Scanning electron micrograph of a β-quartz crystal from the Valley of Ten Thousand Smokes, Alaska, from Clocchiatti (1975). This Hopper-type prism face defect provides a site for melt entrapment as shown by the synthetic melt inclusion in (m).

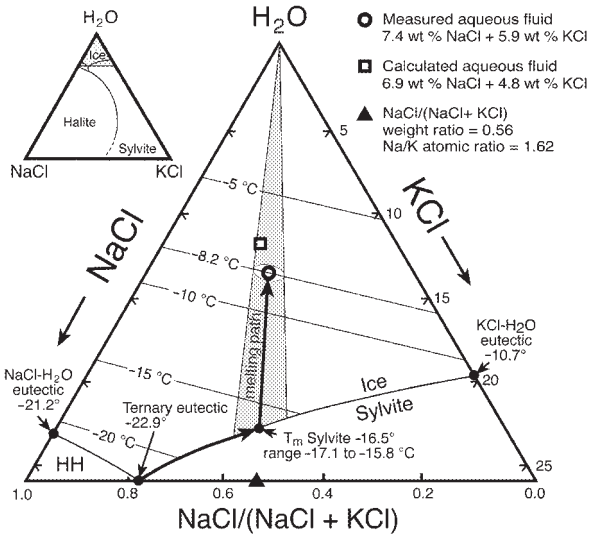

Fig. 4. Portion of the H_2O–KCl–NaCl phase diagram showing the low-temperature phase equilibria (after Hall *et al.*, 1988). Aqueous fluid inclusions ($FIA_{(aq)}$ 1) begin melting at −22·6°C, which is close to the ternary eutectic temperature (−22·9°C). With continued heating, the inclusions follow the ice–sylvite cotectic until sylvite melts between −15·8 and −17·1°C. With continued heating the inclusions follow a path towards the H_2O apex until the last ice crystal melts. The intersection of the melting path with the isotherm corresponding to final ice-melting (−8·2°C) defines the composition of the aqueous solution (7·4 wt % NaCl + 5·9 wt % KCl). The aqueous solution composition was calculated using the FORTRAN program SALTY (Bodnar *et al.*, 1989). Also shown is the composition of the aqueous fluid based on mass balance constraints.

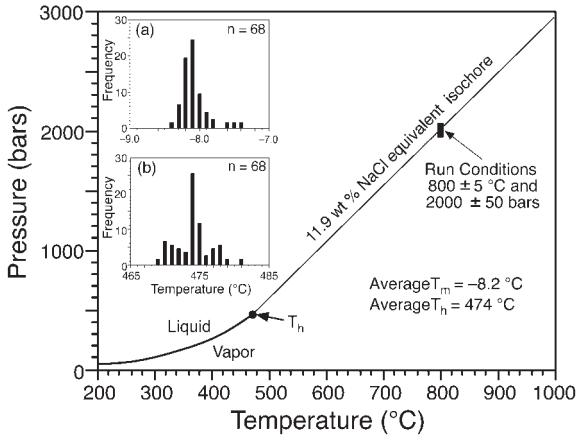

Fig. 5. Microthermometric data for aqueous fluid inclusions ($FIA_{(aq)}$ 1). Final ice-melting temperatures are shown in histogram form in inset (a). Homogenization temperatures are shown in inset (b). The liquid–vapor curve (Liquid/Vapor) for a composition of 11·9 wt % NaCl, and the isochore corresponding to the measured homogenization temperature (T_h) are also shown. The isochore intersects the experimental conditions for formation of the melt and aqueous inclusions, shown by the black rectangle.

SALTY (Bodnar *et al.*, 1989). These same inclusions homogenized to the liquid phase over the temperature range 469–481°C, with a mean temperature of 474°C (Fig. 5, inset b).

Inclusions from $FIA_{(aq)}$ 2 show a wide range in phase ratios at room temperature, and some contain halite crystals at room temperature. In general, inclusions with halite show higher volumes of liquid than vapor (Fig. 3d and e). The majority of the $FIA_{(aq)}$ 2 inclusions are liquid rich and do not contain halite (Fig. 3f); others are nearly all vapor with (Fig. 3g) or without halite. When heated to measure the halite dissolution temperature, all of these inclusions decrepitated at around 200°C as the surrounding matrix glass fractured. Similar behavior was observed for aqueous inclusions in glass by Romano *et al.* (1994). Those workers attributed the fracturing to loss of water from the inclusion to the glass during slow quenching, resulting in differential thermal contraction of the glass immediately surrounding the inclusion compared with the bulk glass. This, in turn, leads to thermal stress in the glass around the inclusion during heating, and subsequent fracturing.

The heterogeneous nature of FIA(aq) 2 fluid inclusions is thought to be a result of disequilibrium processes that occurred during the quench. The high and variable salinities of the inclusions observed in the glass are consistent with the salinities expected for aqueous solutions that exsolve from a silicic melt during 'second boiling' (crystallization and formation of skeletal quartz overgrowths) at a constant pressure of 2 kbar (Cline & Bodnar, 1991). These inclusions thus do not represent the aqueous fluid that was present at run conditions and are not considered further.

Silicate melt inclusions

$FIA_{(mlt)}$ 1 inclusions were heated using four routines to examine the effect of different heating procedures on T_h. In the first example, 16 inclusions from a single quartz wafer were examined, using a heating rate of ~3°C/min with thermal cycling near the homogenization temperature. The inclusions ranged in size from 8 to 30 μm, but 10 of the inclusions had a similar size of ~15 μm in maximum length. Homogenization temperatures ranged from 819 to 839°C with a mean of 833°C (inset as a T_h histogram within Fig. 6). Smaller inclusions typically homogenized at lower temperatures. During heating, the small bubbles (<1 μm) in the largest inclusion collapsed between 590 and 620°C. The reason for the rapid collapse of the small bubbles over a relatively narrow temperature interval is not known, but may be related to (1) solubility of water from vapor bubbles back into the melt, or (2) volume increase as glass transforms to melt at the glass transition temperature, thus eliminating small bubbles. If the latter explanation is the cause of the bubble collapse, it should be noted that the glass transition temperature inferred from this change is higher than is observed

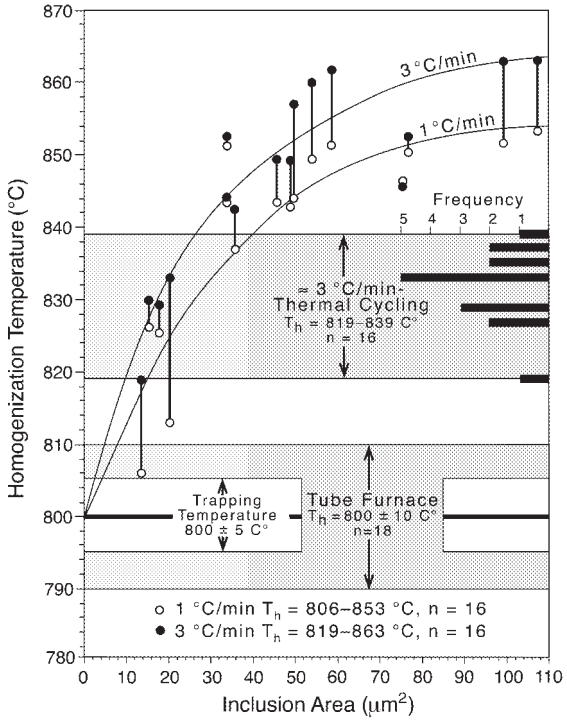

Fig. 6. Summation of T_h results for $FIA_{(mlt)}$ 1 for four different heating routines. The T_h ranges for the tube furnace and the thermal cycling experiments are shown by the shaded boxes, along with the experimental conditions. These experiments did not consider inclusion size. A histogram with frequency vs T_h for the thermal cycling experiment is inset along the right side of the diagram. Inclusion area (as viewed through the microscope) vs T_h for the continuous heating experiments (1°C/min and 3°C/min) are indicated with unfilled and filled circles, respectively. Black vertical tie lines link data for the same inclusion. The continuous line drawn through the data points for the continuous heating experiments shows the general relationship between inclusion size and homogenization temperature, with T_h approaching the trapping temperature as inclusion size approaches zero. The homogenization temperature for the tube furnace experiment coincides most closely with the trapping temperature.

during quenching of the run. A series of photomicrographs showing the changes during heating and subsequent cooling of two inclusions using this heating routine are shown in Fig. 7a and b. It should be noted that the inclusion shown in Fig. 7a before heating (22°C, left photo) shows a mottled appearance owing to the uniform distribution of numerous small quench bubbles throughout the glass, in addition to the larger vapor bubble. After homogenization and quenching back to 22°C (right photo), the inclusion contains only a single vapor bubble that nucleated during the quench.

A second group of 16 inclusions from another quartz wafer was studied using two different constant heating rates above 600°C. The inclusions ranged in size from 6 to 18 μm in maximum length. Using a heating rate of 1°C/min above 600°C, T_h ranged from 806 to 853°C and a positive correlation between inclusion size and homogenization temperature was observed (Fig. 6). The same inclusions were reheated (after cooling to 600°C to renucleate the bubbles) at a rate of 3°C/min and T_h in this experiment ranged from 819 to 863°C. Again, a positive correlation between inclusion size and homogenization temperature was observed (Fig. 6). In the three experiments described above using the heating stage, reappearance of the vapor bubbles occurred between 750 and 650°C during cooling. The new vapor bubble was smaller than the original bubble and in no case did the smaller quench bubbles reappear. These features are thought to be a function of the relatively faster quenching rates (150°C/min) used in the homogenization experiments, compared with the original quench rate (85°C/min) used to cool the cold-seal bombs following inclusion synthesis.

A third quartz wafer with 18 inclusions was incrementally heated in a vertical tube furnace, starting at a temperature of 750°C. The inclusions were 8–20 μm in maximum length. The size of the vapor bubble (as observed after quenching to room temperature) in several inclusions appeared to remain constant from one heating increment to the next, up to 780°C, but decreased notably when heated to 790°C. All inclusions homogenized during the heating step from 790 to 800°C (Fig. 6). During quenching (>800°C/s) the vapor bubbles did not reappear (unlike the results of heating stage experiments).

Composition of melts

Quenched glass inclusions in the quartz wafer from the 1 and 3°C/min heating stage experiments were analyzed by electron microprobe and SIMS after grinding and polishing to expose the inclusion glass. The composition, in terms of albite, orthoclase and quartz, of each inclusion was calculated from oxide totals determined by electron microprobe. These are plotted in Fig. 8 and listed in Table 1. The average composition (in wt %) for nine inclusions is 77·92 SiO_2, 8·93 Al_2O_3, 5·23 K_2O, 2·27 Na_2O, 5·46 H_2O, 0·18 Cl^-. This average composition is used below to represent the equilibrium melt composition ($Ab_{19·2}Or_{31·1}Qtz_{49·1}$) to determine the Na–K partition coefficient between the melt and aqueous fluid. Five melt inclusions were analyzed using SIMS, yielding average water contents of 5·5 wt % and Cl^- contents of 0·18 wt %. Spot electron microprobe analyses were also obtained from clear haplogranite matrix glass adjacent to the quartz core and adjacent to quartz microphenocrysts. Compositions of this glass range from the average of the glass inclusions to a more silica-depleted composition of $Ab_{26}Or_{38}Qtz_{35}$ (Fig. 8). The trend in glass compositions from the average composition of melt inclusions towards the cotectic shown in Fig. 8 is consistent with that predicted by Tuttle & Bowen (1958) for melts undergoing

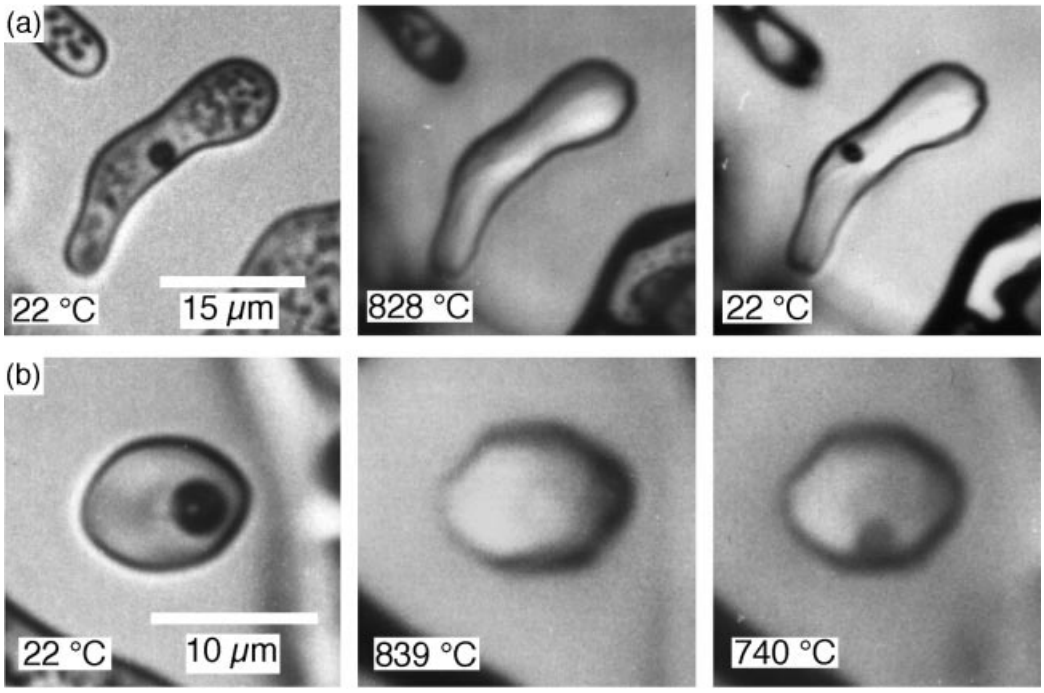

Fig. 7. Behavior during heating for two glass inclusions. (a) Oblong melt inclusion containing numerous small quench bubbles and a single large vapor bubble at 22°C (left), at the homogenization temperature (828°C, center), and after quenching back to 22°C (right). (Note the presence of only a single vapor bubble after homogenization and quenching.) (b) Negative-crystal form melt inclusion containing a single vapor bubble at 22°C (left). The center image shows the inclusion at the homogenization temperature (839°C), and the right image shows the inclusion during quenching, at the approximate temperature (740°C) at which the vapor bubble reappeared.

quartz crystallization (as evidenced by skeletal overgrowths on quartz microphenocrysts) during isobaric cooling. The composition of $FIA_{(mlt)}$ 2 inclusions was not determined because these inclusions presumably formed during the quench and thus do not represent the melt present at run conditions.

INTERPRETATION

Melt and aqueous fluid compositions

$FIA_{(aq)}$ 1 and $FIA_{(mlt)}$ 1 inclusions trapped in the quartz core were used to determine the equilibrium compositions of the immiscible silicate melt and aqueous fluids at 800°C and 2000 bars. Based on the average final ice-melting temperature (−8·2°C), the $FIA_{(aq)}$ 1 inclusions had a salinity of 11·9 wt % NaCl equivalent. The average homogenization temperature of these same inclusions was 474°C. The isochore for a fluid inclusion with this composition and homogenization temperature passes through the *P–T* run conditions (Fig. 5), providing strong evidence that the fluid inclusions do contain samples of the aqueous fluid present at run conditions and that the inclusions have not been altered during the quench. It should be noted that the isochore shown in Fig. 5 is the isochore for an NaCl–H_2O fluid composition (11·9 wt %) corresponding to the measured ice-melting temperature of the aqueous inclusions (–8·2°C), and not the isochore for the fluid composition (7·4 wt % NaCl + 5·9 wt % KCl = 13·3 wt % total salt) determined from sylvite and ice-melting temperatures of the inclusions. The reasons for using the isochore corresponding to the ice-melting temperature are as follows. First, *PVT* data for the system H_2O–NaCl–KCl do not exist for high temperatures and pressures. Second, Bodnar (1983) has shown that the *PVT* properties of mixed aqueous electrolyte solutions are approximated reasonably well by the *PVT* properties of an H_2O–NaCl solution having the same freezing-point depression (ice-melting temperature) as the mixed electrolyte.

The average composition of the glass inclusions plots on the 2000 bar, 800°C isotherm in the Ab–Or–Qtz–H_2O 'ternary' system (Fig. 8, inset), providing convincing evidence that the melt inclusions contain a sample of the melt that was present, and in equilibrium with the aqueous phase, at run conditions. Thus, the properties and behavior of the aqueous and melt inclusions are both consistent with having been trapped at 800°C and 2000 bars in the haplogranite–H_2O–(NaCl–KCl) system, and may be used to study the behavior during heating of melt inclusions of known composition and formation conditions. It is also worth noting the excellent agreement

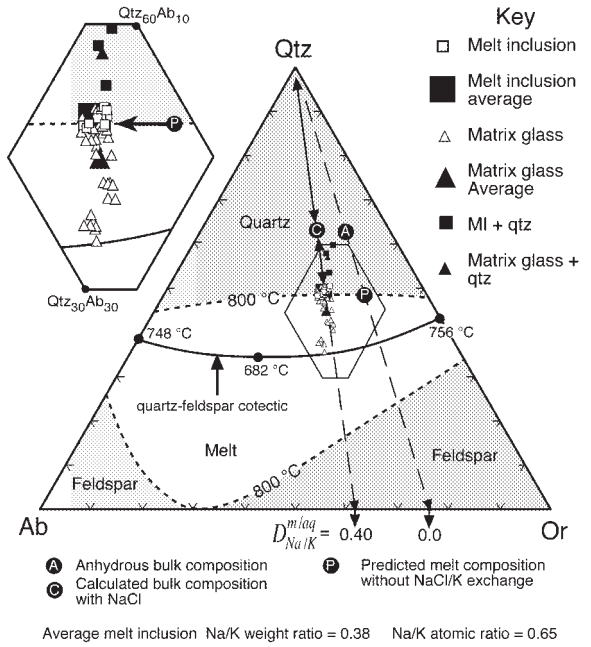

Fig. 8. Matrix glass and $FIA_{(mlt)}$ 1 inclusion compositions plotted on the 2000 bar H_2O-saturated haplogranite ternary as described for Fig. 1. Compositions were determined for nine melt inclusions from the quartz core and for 42 matrix glass locations. Data points labeled MI + qtz and Matrix glass + qtz represent analyses in which the beam intersected both glass and quartz. Data are listed in Table 1. Also shown are the initial starting composition for the non-aqueous components (point 'A'), the expected melt composition in the NaCl-free, H_2O-saturated haplogranite system assuming no exchange of sodium and potassium between melt and aqueous fluid (point 'P'), and the calculated starting composition including NaCl from the aqueous phase (point 'C'). The Na–K distribution coefficient for the system assuming no exchange of sodium and potassium between the melt and aqueous solution ($D^{m/aq}_{Na/K} = 0{\cdot}0$), and the calculated distribution coefficient based on the measured melt and aqueous inclusion compositions ($D^{m/aq}_{Na/K} = 0{\cdot}40$) are also shown.

between our results and those of Tuttle & Bowen (1958), even though they used 'pure' water in their experiments whereas we used a 10 wt % NaCl aqueous solution. If the aqueous solution exhibits ideal behavior at experimental conditions, the activity of H_2O in our experiments would have been 0·96. Moreover, Webster (1992) reported that as the alkali chloride concentration in the aqueous phase increases, the activity coefficient for water in the aqueous fluid exhibits increasingly positive deviations from ideality, indicating that the calculated activity of 0·96 based on ideal behavior represents a minimum water activity. Thus, the water activity in our aqueous chloride solutions may not have been much different from that of the 'pure' water experiments of Tuttle & Bowen (1958).

It should be noted that the compositions of the melt inclusions and the matrix glass (Fig. 8) do not fall along the pseudobinary that passes through the original starting composition (point 'A', Fig. 8). Rather, the compositions fall along a pseudobinary representing a melt that is enriched in sodium (or depleted in potassium) relative to the starting composition. This observed shift in the melt composition reflects the exchange of sodium and potassium between the melt and the coexisting aqueous phase at run conditions. (Remember, the aqueous solution loaded into the capsule initially contained only NaCl.)

Using the average melt inclusion Na/K ratio (Fig. 8) and the Na/K ratio of the aqueous fluid determined from sylvite and ice-melting temperatures (Fig. 4), the calculated distribution coefficient ($D^{m/aq}_{Na/K}$) for sodium and potassium exchange between melt and coexisting aqueous chloride solution is 0·40. The analogous partition coefficient for Cl^- between the melt and aqueous solution ($D^{m/aq}_{Cl}$) is 0·021. This value is in agreement with earlier work by Kilinc & Burnham (1972) and Webster (1992), but disagrees with results of Shinohara *et al.* (1989). We note, however, that the melt composition used by Shinohara *et al.* (1989) was considerably more sodium rich than that used here, and Malinin & Kravchuk (1996) reported that chlorine partitioning between melt and fluid depends on the Na/K ratio of the melt.

The H_2O content of melt inclusions determined by SIMS ranges from 4·83 to 6·35 wt % ($n = 5$), with an average of 5·5 wt %. The experimentally determined water solubility at 2 kbar and 800°C in a haplogranite melt with a composition ($Ab_{19{\cdot}05}Or_{35{\cdot}86}Qtz_{45{\cdot}85}NaMS_{0{\cdot}23}$) similar to that of the melt inclusions is 5·63 wt % (Holtz *et al.*, 1992). The water solubility in a melt with the average composition for the melt inclusions, calculated using the Burnham model (Burnham, 1979) is 5·33 wt %. Thus, the experimentally determined and calculated water solubilities are in good agreement with the measured water content of the melt inclusions, suggesting that there has been little or no water loss during quenching.

Melt inclusion formation conditions

Previous workers have used results obtained from presumably coeval melt and aqueous fluid inclusions to constrain the temperature and pressure of formation of the inclusions (Naumov *et al.*, 1992, 1996; Yang & Bodnar, 1994; Thomas, 1994*a*). The assumptions upon which this technique are based are that (1) the aqueous fluid inclusion isochore passes through the *P–T* formation conditions and (2) the temperature of formation of the melt inclusions is equal to their homogenization temperature, i.e. the melt inclusions were trapped on the water-saturated solidus. Thomas (1994*b*) considered examples where the melt inclusions are not trapped on the water-saturated solidus. We have already seen (Fig. 5) that the aqueous inclusion isochore for our synthetic inclusions does indeed pass through the formation *P–T* conditions. Thus, use of microthermometric data from coeval aqueous and melt inclusions becomes a matter of determining

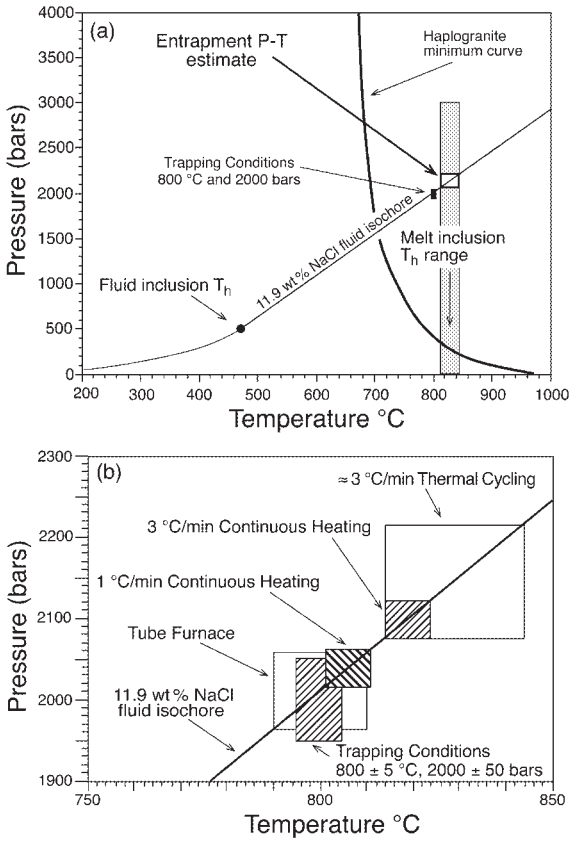

Fig. 9. Estimated *P–T* formation conditions for the coexisting melt and aqueous synthetic inclusions of this study, calculated using vapor–melt homogenization temperatures for the four different homogenization heating experiments. (a) *P–T* estimate for the ~3°C/min thermal cycling heating experiment, showing the aqueous inclusion liquid–vapor curve and isochore to illustrate the 'intersecting isochore' technique (Roedder & Bodnar, 1980) used to determine formation conditions. (b) *P–T* estimates for the four different homogenization heating experiments. (See text for details.)

the 'correct' homogenization temperature for the melt inclusions. In this study we have attempted to identify the most reliable technique for determining T_h, as well as the factors that affect that measurement.

In the first homogenization experiment, thermal cycling was used to determine T_h, and heating was not continuous. The T_h determined for melt inclusions ranged from 819 to 839 $\pm$ 5°C. If this temperature range (814–844°C) were used to represent the homogenization (and trapping) temperature of the melt, the predicted trapping pressure would be 2073–2212 bars, as shown in Fig. 9a and b.

In the second and third homogenization experiments, the heating rates were constant at 1 and 3°C/min, respectively, during homogenization of the melt inclusions. Thermal cycling was not used for homogenization confirmation. The lack of thermal cycling may result in apparent homogenization temperatures that are less than the actual homogenization temperature by a few degrees. For these two experiments, the T_h of the smallest inclusion was selected for entrapment pressure and temperature estimates because, on the basis of results shown in Fig. 6, this temperature most closely represents the 'true' homogenization temperature, which, for inclusions trapped at water saturation, also equals the actual formation temperature. Results presented by Thomas (1994*a*) also indicate that apparent T_h measurements for smaller inclusions are lower than those for coeval larger inclusions (see also Sobolev & Kostyuk, 1975). In the 1°C/min heating experiment, the lowest T_h was 806 $\pm$ 5°C. The intersection of the aqueous fluid inclusion isochore with this temperature range predicts entrapment at 801–811°C and 2012–2058 bars (Fig. 9b). In the 3°C/min heating experiment, the lowest T_h was 819 $\pm$ 5°C. The intersection of the aqueous fluid inclusion isochore with this T_h range gives formation conditions of 814–824°C and 2073–2119 bars (Fig. 9b).

Finally, T_h was determined through incremental heating in a tube furnace using 10°C/day heating increments. Vapor–melt homogenization was observed at 800 $\pm$ 10°C for all inclusions. The predicted entrapment estimate is 790–810°C and 1961–2054 bars (Fig. 9b). This formation condition estimate is in excellent agreement with the run conditions (which also represent the trapping conditions).

DISCUSSION AND SUMMARY

Lowenstern (1994) and Thomas (1994*a*, 1994*b*) reported that homogenization measurements obtained from natural inclusions using a heating stage differed by as much as 75°C from values obtained using a tube furnace. Both studies suggested that heating rates are important variables that can significantly affect the measured homogenization temperature. Those workers suggested that the relationship between heating rate and apparent homogenization temperature reflected the fact that diffusion of volatiles in melt inclusions is too slow to maintain a homogeneous volatile composition throughout the melt with the relatively fast heating rates used in microthermometry. Thus, as the solubility of the volatile phase in the melt increases as temperature and, especially, pressure increase during the heating experiment, volatiles from the vapor bubble are unable to diffuse through the melt sufficiently fast to maintain a homogeneous (equilibrium) composition. As such, the homogenization temperatures obtained using microscope heating stages often exceed the true homogenization temperature. One could ask then: 'Why don't workers simply use slower heating rates when using microscope heating stages?' In principle, this is possible, but problems with oxidation during long duration heating runs, as well as potential damage to the microscope

optics from the high temperatures, discourage most workers from conducting long-term heating experiments using microscope heating stages.

Results presented here confirm suggestions by other workers that the smallest inclusions and the slowest heating rate most accurately predict the actual entrapment temperature. Further, our results prove that in immiscible silicate melt–aqueous fluid systems the pressure of entrapment can be accurately predicted using isochores determined from microthermometric measurements of aqueous fluid inclusions and homogenization temperatures obtained from coeval silicate melt inclusions. Our results also suggest that, in general, T_h values determined using microscope heating stages (with relatively fast heating rates) will exceed the 'true' T_h value. This statement applies most directly to silicate melt inclusions that trap a water-saturated melt. If the inclusion traps a water-undersaturated melt, the measured T_h may be less than the trapping temperature because the vapor bubble will disappear before the trapping temperature is reached (see Lowenstern, 1995, fig. 4). Similarly, if the hydrous melt crystallizes during cooling, the P–T path followed during subsequent heating to measure T_h may produce internal pressures in the inclusions that are well in excess of the original trapping pressure, and may cause decrepitation before the homogenization temperature is reached (Student & Bodnar, 1996).

When using a microscope heating stage to measure homogenization temperatures, workers should select the smallest inclusions for study. Using a constant heating rate, the apparent T_h approaches the true homogenization temperature as the inclusion size approaches zero. The use of small inclusions does, however, have disadvantages, including the increased difficulty of making accurate observations under the microscope and the larger uncertainties in composition that result as the inclusion size approaches the analytical area (or volume) of the microanalytical instrument [electron microprobe, SIMS, laser inductively coupled plasma mass spectrometry (ICP-MS)]. Additionally, boundary layer effects, leading to melt inclusion compositions that may differ from the bulk melt composition, become more problematical as inclusion size decreases (Lowenstern, 1995). Alternatively, incremental heating in a tube furnace provides accurate T_h determinations that are not size dependent (if the sample is maintained at an elevated temperature for a sufficiently long period of time, i.e. 24 h). Thomas (1994*c*) did, however, observe a size dependence for crystallized melt inclusions heated in a 1 atm furnace. It should be noted that 1 atm heating runs of long duration may lead to severe oxidation of samples [owing to hydrogen loss from the melt by diffusion through the host phase at high temperature (Mavrogenes & Bodnar, 1994)], especially those containing significant amounts of iron, and may be unreliable if the homogenized melt phase cannot be quenched to a single-phase, homogeneous (crystal-free) glass.

Perhaps the most important result of this study is the observation that glass and aqueous inclusions trapped in the quartz core contain samples of the melt and aqueous solution that were in equilibrium at run conditions. Moreover, both the melt and aqueous inclusions maintain their compositions (and volumetric properties) during quenching to room temperature and may be used to study the distribution of components between melt and fluid phases. Aqueous inclusions trapped in quartz do not lose water to the host phase during the quench, as do similar inclusions in glass (see Romano *et al.*, 1994), and the aqueous phase does not undergo ion exchange with the host, thus changing the fluid composition during the quench (Shinohara *et al.*, 1989). Further, the aqueous inclusions in the quartz core ($FIA_{(aq)}$ 1) maintain volumetric properties representative of original formation conditions, and do not continue to change volume during cooling to the glass transition temperature (Romano *et al.*, 1994). As a result, the isochore for aqueous inclusions in the quartz core passes through the formation conditions, rather than through the glass transition temperature, permitting determination of the original formation conditions.

Because it is possible to trap representative samples of both the liquid and the vapor phases in immiscible aqueous fluid systems (Bodnar *et al.*, 1985), the technique described here may be used to study the important problem of metal partitioning in crystal–melt–liquid–vapor systems. At present, the concentrations of metals and other components in the coexisting aqueous phases are calculated based on previously determined chlorine concentrations of the immiscible phases, using the metal concentration in the bulk fluid measured after quenching (see Webster, 1992; Candela & Piccoli, 1995; Williams *et al.*, 1995). However, use of the synthetic fluid inclusion technique described above (specifically, trapping the inclusions in quartz or some other 'inert' crystal host rather than in glass), combined with microanalytical techniques such as synchrotron X-ray fluorescence (Mavrogenes *et al.*, 1995) or laser-ablation ICP-MS (Audétat *et al.*, 1998) for individual inclusion analysis, may permit the direct sampling and analysis of fluids that were in equilibrium at run conditions, eliminating the need to calculate fluid compositions. Trapping samples of the coexisting phases at run conditions in a relatively impermeable and inert crystal bottle (quartz) eliminates, or at least minimizes, the possibility that the compositions will be altered during quenching and extraction of the sample from the capsule.

ACKNOWLEDGEMENTS

Discussions with C. Szabo and M. Rapien over the course of this study contributed significantly to our under-

standing of melt inclusion behavior. J.J.S. thanks C. U. Schmidt for assistance with experimental techniques. T. Solberg is thanked for developing techniques for the accurate analysis of glass by electron microprobe. Detailed comments and suggestions by Jake Lowenstern and two anonymous reviewers significantly improved the manuscript, and are greatly appreciated. Erik Hauri of the Department of Terrestrial Magnetism provided access to the SIMS facilities and assistance with interpretation of analytical data. Funding for this research was provided by NSF Grants EAR-9305032 and EAR-9527034 to R.J.B.

REFERENCES

Anderson, A. T., Jr (1974). Evidence for a picritic, volatile-rich magma beneath Mt Shasta, California. *Journal of Petrology* **15,** 243–267.

Anderson, A. T., Jr (1991). Hourglass inclusions: theory and application to the Bishop rhyolitic tuff. *American Mineralogist* **76,** 530–547.

Audétat, A., Günther, D. & Heinrich, C. A. (1998). Formation of a magmatic–hydrothermal ore deposit: insights with LA-ICP-MS analysis of fluid inclusions. *Science* **279,** 2091–2094.

Bodnar, R. J. (1983). A method of calculating fluid inclusion volumes based on vapor bubble diameters and *P–V–T–X* properties of inclusion fluids. *Economic Geology* **78,** 535–542.

Bodnar, R. J. (1993). Revised equation and table for determining the freezing point depression of H_2O–NaCl solutions. *Geochimica et Cosmochimica Acta* **57,** 683–684.

Bodnar, R. J. & Sterner, S. M. (1987). Synthetic fluid inclusions. In: Ulmer, G. C. & Barnes, H. L. (eds) *Hydrothermal Experimental Techniques*. New York: John Wiley, pp. 423–457.

Bodnar, R. J. & Vityk, M. O. (1994). Interpretation of microthermometric data for H_2O–NaCl fluid inclusions. In: De Vivo, B. & Frezzotti, M. L. (eds) *Fluid Inclusions in Minerals: Methods and Applications*. Blacksburg, VA: Virginia Tech, pp. 117–130.

Bodnar, R. J., Burnham, C. W. & Sterner, S. M. (1985). Synthetic fluid inclusions in natural quartz. III. Determination of phase equilibrium properties in the system H_2O–NaCl to 1000°C and 1500 bars. *Geochimica et Cosmochimica Acta* **49,** 1861–1873.

Bodnar, R. J., Sterner, S. M. & Hall, D. L. (1989). SALTY: a FORTRAN program to calculate compositions of fluid inclusions in the system NaCl–KCl–H_2O. *Computers and Geosciences* **15,** 19–41.

Burnham, C. W. (1979). Magmas and hydrothermal fluids. In: Barnes, H. L. (ed.) *Geochemistry of Hydrothermal Ore Deposits*. New York: John Wiley, pp. 71–136.

Burnham, C. W. & Jahns, R. H. (1962). A method for determining the solubility of water in silicate melts. *American Journal of Science* **260,** 721–745.

Candela, P. A. & Piccoli, P. M. (1995). Model ore–metal partitioning from melts into vapor and vapor–brine mixtures. In: Thompson, J. F. H. (ed.) *Magmas, Fluids and Ore Deposits. Mineralogical Association of Canada, Short Course* **23,** 101–127.

Cline, J. S. & Bodnar, R. J. (1991). Can economic porphyry copper mineralization be generated by a typical calc-alkaline melt? *Journal of Geophysical Research* **96,** 8113–8126.

Clocchiatti, R. (1975). Les inclusions vitreuses des cristaux de quartz: étude optique, thermo-optique et chimique; applications géologiques. *Société Géologique de France, Mémoires (Nouvelle Serie)* **54**(122), 1–96.

Davis, M. J. & Ihinger, P. D. (1998). Heterogeneous crystal nucleation on bubbles in silicate melt. *American Mineralogist* **83,** 1008–1015.

Frezzotti, M. L. (1992). Magmatic immiscibility and fluid phase evolution in the Mount Genis granite (southeastern Sardinia, Italy). *Geochimica et Cosmochimica Acta* **56,** 21–33.

Goldstein, R. H. & Reynolds, T. J. (1994). *Systematics of Fluid Inclusions in Diagenetic Minerals. SEPM Short Course* **31,** 199 pp.

Hall, D. L., Sterner, S. M. & Bodnar, R. J. (1988). Freezing point depression of NaCl–KCl–H_2O solutions. *Economic Geology* **83,** 197–202.

Hamilton, D. L. & Henderson, C. M. B. (1968). The preparation of silicate compositions by a gelling method. *Mineralogical Magazine* **36,** 832–838.

Hansteen, T. H. & Lustenhouwer, W. J. (1990). Silicate melt inclusions from a mildly peralkaline granite in the Oslo paleorift, Norway. *Mineralogical Magazine* **54,** 195–205.

Hauri, E., Wang, J., Dixon, J. E. & Newman, S. (1999). SIMS investigations of volatiles in volcanic glasses 1: Calibration, sensitivity and comparisons with FTIR. *Chemical Geology* (in press).

Holtz, F., Behrens, H., Dingwell, D. B. & Taylor, R. P. (1992). Water solubility in aluminosilicate melts of haplogranite composition at 2 kbar. *Chemical Geology* **96,** 289–302.

Kilinc, I. A. & Burnham, C. W. (1972). Partitioning of chloride between a silicate melt and coexisting aqueous phase from 2 to 8 kilobars. *Economic Geology* **67,** 231–235.

Koster van Groos, A. F. & Wyllie, P. J. (1969). Melting relationships in the system $NaAlSi_3O_8$–NaCl–H_2O at one kilobar pressure, with petrologic applications. *Journal of Geology* **77,** 581–606.

Lowenstern, J. B. (1994). Chlorine, fluid immiscibility, and degassing in peralkaline magmas from Pantelleria, Italy. *American Mineralogist* **79,** 353–369.

Lowenstern, J. B. (1995). Applications of silicate–melt inclusions to the study of magmatic volatiles. In: Thompson, J. F. H. (ed.) *Magmas, Fluids and Ore Deposits. Mineralogical Association of Canada, Short Course* **23,** 71–99.

Malinin, S. D. & Kravchuk, I. F. (1996). Behavior of chlorine in equilibria between silicate melts and aqueous chloride fluids. *Geochemistry International* **33,** 49–71.

Mavrogenes, J. A. & Bodnar, R. J. (1994) Hydrogen movement into and out of fluid inclusions in quartz: experimental evidence and geologic implications. *Geochimica et Cosmochimica Acta* **58,** 141–148.

Mavrogenes, J. A., Bodnar, R. J., Anderson, A. J., Bajt, S., Sutton, S. R. & Rivers, M. L. (1995). Assessment of the uncertainties and limitations of quantitative elemental analysis of individual fluid inclusions using synchrotron X-ray fluorescence. *Geochimica et Cosmochimica Acta* **59**(19), 3987–3995.

Naumov, V., Kovalenker, V., Rusinov, V., Solovova, I. & Kamen, M. (1992). High density fluid inclusions of magmatic water in phenocrysts from rhyolite of the Stiavnica stratovolcano (Central Slovakia). *Geologica Carpathica* **43,** 85–89.

Naumov, V. B., Tolstykh, M. L., Kovalenker, V. A. & Konokova, N. N. (1996). Fluid overpressure in andesite melts from Central Slovakia: evidence from inclusions in minerals. *Petrology* **4,** 265–276.

Pouchou, J. L. & Pichoir, F. (1985). 'PAP' procedure to improve quantitative microanalysis. *Microbeam Analysis* **20,** 104–105.

Roedder, E. (1979). Origin and significance of magmatic inclusions. *Bulletin de Minéralogie* **102,** 487–510.

Roedder, E. (1984). *Fluid Inclusions*. Washington, DC: Mineralogical Society of America, 644 pp.

Roedder, E. (1992). Fluid inclusion evidence for immiscibility in magmatic differentiation. *Geochimica et Cosmochimica Acta* **56,** 5–20.

Roedder, E. & Bodnar, R. J. (1980). Geologic pressure determinations from fluid inclusion studies. *Annual Review of Earth and Planetary Sciences* **8,** 263–301.

Romano, C., Dingwell, D. B. & Sterner, S. M. (1994). Kinetics of quenching of hydrous feldspathic melts: quantification using synthetic fluid inclusions. *American Mineralogist* **79,** 1125–1134.

Shinohara, H., Iiyama, J. T. & Matsuo, S. (1989). Partition of chlorine compounds between silicate melt and hydrothermal solutions: I. Partition of NaCl–KCl. *Geochimica et Cosmochimica Acta* **53,** 2617–2630.

Sobolev, V. S. & Kostyuk, V. P. (1975). *Magmatic Crystallization Based on a Study of Melt Inclusions*. Novosibirsk: Nauka (in Russian). [Translated in: Roedder, E. & Kozlowski, A. (eds) (1976). *Fluid Inclusion Research, Volume 9*. Ann Arbor, MI: University of Michigan Press, pp. 182–253.]

Sterner, S. M. & Bodnar, R. J. (1984). Synthetic fluid inclusions in natural quartz. I. Compositional types synthesized and applications to experimental geochemistry. *Geochimica et Cosmochimica Acta* **48,** 2659–2668.

Sterner, S. M., Hall, D. L. & Bodnar, R. J. (1988). Synthetic fluid inclusions. V. Solubility relations in the system NaCl–KCl–H_2O under vapor-saturated conditions. *Geochimica et Cosmochimica Acta* **52,** 989–1005.

Student, J. J. & Bodnar, R. J. (1996). Melt inclusion microthermometry: petrologic constraints from the H_2O-saturated haplogranite system. *Petrology* **4,** 291–306.

Thomas, R. (1994*a*). Estimation of water content of granitic melts from inclusion data. In: Seltmann, R., Kampf, H. & Moller, P. (eds) *Metallogeny of Collisional Orogens Focused on the Erzgebirge and Comparable Metallogenetic Settings*. Prague: Czech Geological Survey, pp. 224–229.

Thomas, R. (1994*b*). Fluid evolution in relation to the emplacement of the Variscan granites in the Erzgebirge region: a review of the melt and fluid inclusion evidence. In: Seltmann, R., Kampf, H. & Moller, P. (eds) *Metallogeny of Collisional Orogens Focused on the Erzgebirge and Comparable Metallogenetic Settings*. Prague: Czech Geological Survey, pp. 70–81.

Thomas, R. (1994*c*). Estimation of the viscosity and the water content of silicate melts from melt inclusion data. *European Journal of Mineralogy* **6,** 511–535.

Tuttle, O. F. & Bowen, N. L. (1958). Origin of granite in the light of experimental studies in the system $NaAlSi_3O_8$–$KAlSi_3O_8$–SiO_2–H_2O. *Geological Society of America Memoir* **74,** 1–153.

Voigt, D. E., Bodnar, R. J. & Blencoe, J. G. (1981). Water solubility in melts of alkali feldspar composition at 5 kbar and 950°C (abstract). *EOS Transactions, American Geophysical Union* **62,** 428.

Webster, J. D. (1992). Water-solubility and chlorine partitioning in Cl-rich granitic systems: effects of melt composition at 2 kbar and 800°C. *Geochimica et Cosmochimica Acta* **56,** 679–687.

Werre, R. W., Jr, Bodnar, R. J., Bethke, P. M. & Barton, P. B., Jr (1979). A novel gas-flow fluid inclusion heating/freezing stage (abstract). *Geological Society of America, Abstracts with Programs* **11,** 539.

Williams, T. J., Candela, P. A. & Piccoli, P. M. (1995). The partitioning of copper between silicate melts and two-phase aqueous fluids: an experimental investigation at 1 kbar, 800°C and 0·5 kbar, 850°C. *Contributions to Mineralogy and Petrology* **121,** 388–399.

Yang, K. & Bodnar, R. J. (1994). Why is economic porphyry copper mineralization absent from the granitoids of the Gyeongsang Basin, South Korea? Evidence from silicate melt and aqueous fluid inclusions. *International Geology Review* **36,** 608–628.